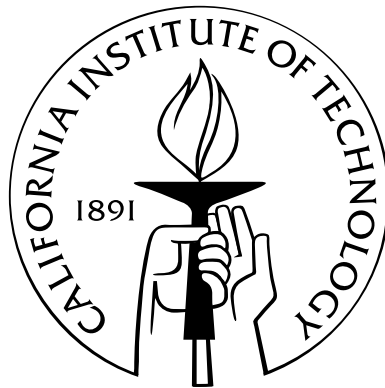


Optoelectronic Control of the Phase and Frequency of Semiconductor Lasers

Thesis by
Naresh Satyan

In Partial Fulfillment of the Requirements
for the Degree of
Doctor of Philosophy



California Institute of Technology
Pasadena, California

2011
(Defended May 16, 2011)

© 2011

Naresh Satyan

All Rights Reserved

In loving memory of Dilip

Acknowledgements

I am grateful for the support, encouragement, and friendship of a large number of people who have made my stay at Caltech productive and enjoyable.

I am thankful to Prof. Amnon Yariv for the opportunity to be a member of his research group, and the freedom to grow as a researcher. He has always been a source of inspiration with his intuition and insight, and being part of his group has allowed me to interact with, and learn from, a number of knowledgeable and talented individuals.

A large part of this work has been collaborative, and I thank the number of researchers with whom I have benefited from working. Dr. Wei Liang was instrumental in helping me develop a good understanding of the theoretical and experimental aspects of optical phase-locked loops. I have enjoyed numerous brainstorming sessions with Dr. George Rakuljic, discussing new ideas and their feasibility and relevance to the real world. I have learned much about experimental system design from Dr. Anthony Kewitsch. More recently, I have enjoyed exploring various facets of optoelectronic control with Arseny Vasilyev, Jacob Sendowski, and Yasha Vilenchik. I have also had the pleasure of collaborating with other groups on some aspects of this work: Firooz Aflatouni and Prof. Hossein Hashemi at the University of Southern California designed custom integrated circuits to phase-lock semiconductor lasers; and Jason Gamba and Prof. Richard Flagan at Caltech helped us demonstrate the feasibility of using our laser sources for biomolecular sensing.

I thank the many current and past members of the research group with whom I have had fruitful interactions. Dr. John Choi and I spent too many hours together in the office, and he taught me how to be an experimentalist. Dr. Reginald Lee

has provided stimulating conversations and expert advice every week. I have enjoyed technical and other discussions with Prof. Bruno Crosignani, Prof. Joyce Poon, Prof. Lin Zhu, Dr. Philip Chak, Prof. Avi Zadok, Dr. Xiankai Sun, Hsi-Chun Liu, Christos Santis, Scott Steger, James Raftery and Sinan Zhao. I owe special thanks to Connie Rodriguez for her thoughtfulness and hard work in looking after us. I also thank Alireza Ghaffari, Kevin Cooper and Mabel Chik for their support.

I thank Profs. Bruno Crosignani, Ali Hajimiri, Kerry Vahala, and Changhui Yang for serving on my candidacy and thesis committees.

I am fortunate to have formed many friendships at Caltech that have helped me explore my interests outside work. Phanish Suryanarayana, Pinkesh Patel, Setu Mohta, and Devdutt Marathe have been wonderful roommates. I have greatly enjoyed the Carnatic music sessions with Shankar Kalyanaraman, Prabha Mandayam and Chithra Krishnamurthy. John Choi and Philip Tsao have introduced me to bad movies and good food. I have enjoyed many great times—on and off the cricket field—with the large Indian contingent at Caltech: Tejaswi Navilarekallu, Abhishek Tiwari, Vijay Natraj, Sowmya Chandrasekar, Krish Subramaniam, Swaminathan Krishnan, Shaunak Sen, Vikram Deshpande, Vikram Gavini, Abhishek Saha, Anu and Ashish Mahabal, Sonali and Vaibhav Gadre, Mayank Bakshi, Mansi Kasliwal, Zeeshan Ahmed, Uday Khankhoje, Ravi Teja Sukhavasi, Bharat Penmecha, Varun Bhalerao, Shriharsh Tendulkar and Srivatsan Hulikal. Thanks to all my regular hiking partners over the years: the Caltech Y, members of my research group, Shankar Kalyanaraman, Mayank Bakshi, Gautham Jayaram, and especially to Tejaswi Navilarekallu, Pinkesh Patel and Shriharsh Tendulkar. Thanks also to Saurabh Vyawahare and Shankar Kalyanaraman for their company on the long bike rides. I made the decision to live in the Los Angeles area without a car, and I owe many thanks (and apologies) to friends inconvenienced by this on occasion.

Finally, I am deeply thankful for the love, support, and understanding of my parents and my family.

Abstract

This thesis explores the precise control of the phase and frequency of the output of semiconductor lasers (SCLs), which are the basic building blocks of most modern optical communication networks. Phase and frequency control is achieved by purely electronic means, using SCLs in optoelectronic feedback systems, such as optical phase-locked loops (OPLLs) and optoelectronic swept-frequency laser (SFL) sources. Architectures and applications of these systems are studied.

OPLLs with single-section SCLs have limited bandwidths due to the nonuniform SCL frequency modulation (FM) response. To overcome this limitation, two novel OPLL architectures are designed and demonstrated, viz. (i) the sideband-locked OPLL, where the feedback into the SCL is shifted to a frequency range where the FM response is uniform, and (ii) composite OPLL systems, where an external optical phase modulator corrects excess phase noise. It is shown, theoretically and experimentally, and in the time and frequency domains, that the coherence of the master laser is “cloned” onto the slave SCL in an OPLL. An array of SCLs, phase-locked to a common master, therefore forms a coherent aperture, where the phase of each emitter is electronically controlled by the OPLL. Applications of phase-controlled apertures in coherent power-combining and all-electronic beam-steering are demonstrated.

An optoelectronic SFL source that generates precisely linear, broadband, and rapid frequency chirps (several 100 GHz in 0.1 ms) is developed and demonstrated using a novel OPLL-like feedback system, where the frequency chirp characteristics are determined solely by a reference electronic oscillator. Results from high-sensitivity biomolecular sensing experiments utilizing the precise frequency control are reported. Techniques are developed to increase the tuning range of SFLs, which is the primary

requirement in high-resolution three-dimensional imaging applications. These include (i) the synthesis of a larger effective bandwidth for imaging by “stitching” measurements taken using SFLs chirping over different regions of the optical spectrum; and (ii) the generation of a chirped wave with twice the chirp bandwidth and the same chirp characteristics by nonlinear four-wave mixing of the SFL output and a reference monochromatic wave. A quasi-phase-matching scheme to overcome dispersion in the nonlinear medium is described and implemented.

Contents

List of Figures	xii
List of Tables	xx
Glossary of Acronyms	xxi
1 Overview	1
1.1 Introduction	1
1.2 Optical Phase-Locked Loops (OPLLs) and Applications	2
1.3 Optoelectronic Swept-Frequency Lasers (SFLs)	4
1.4 Organization of the Thesis	6
2 Semiconductor Laser Optical Phase-Locked Loops	8
2.1 OPLL Basics	8
2.1.1 Small-Signal Analysis	12
2.1.2 OPLL Performance Metrics	14
2.2 Performance of Different OPLL Architectures	16
2.2.1 Type I OPLL	17
2.2.2 Type I, Second-Order OPLL	19
2.2.3 Type I OPLL with Delay	21
2.2.4 Type II Loop with Delay	23
2.3 FM Response of Single-Section SCLs	27
2.4 OPLL Filter Design	28
2.5 Phase-Locking of Commercial SCLs	31

2.6	Novel Phase-Lock Architectures I: Sideband Locking	35
2.6.1	Principle of Operation	36
2.6.2	Experimental Demonstration	38
2.7	Novel Phase-Lock Architectures II: Composite OPLLs	42
2.7.1	System Description	42
2.7.1.1	Double-Loop Configuration	42
2.7.1.2	Composite PLL	45
2.7.2	Results	47
2.7.2.1	Laser Frequency Modulation Response	47
2.7.2.2	Numerical Calculations	47
2.7.2.3	Experimental Validation	51
2.7.3	Summary	54
3	Coherence Cloning using SCL-OPLLs	55
3.1	Introduction	55
3.2	Notation	56
3.3	Coherence Cloning in the Frequency Domain	57
3.3.1	Experiment	57
3.3.2	Coherence Cloning and Interferometer Noise	60
3.3.2.1	Coherence Cloning Model	61
3.3.2.2	Spectrum of the Laser Field	64
3.3.2.3	Spectrum of the Detected Photocurrent	68
3.3.3	Summary	72
3.4	Time-Domain Characterization of an OPLL	72
3.4.1	Experiment	74
3.4.1.1	Allan Variance and Stability	75
3.4.1.2	Residual Phase Error, Revisited	79
3.4.2	Summary	80
4	Phase-Controlled Apertures	82
4.1	Coherent Power-Combining	82

4.1.1	Experiment	84
4.1.2	Phase Control Using a VCO	86
4.1.2.1	Steady-State Analysis	88
4.1.2.2	Small-Signal Analysis	91
4.1.3	Combining Efficiency	93
4.1.4	Summary	96
4.2	Optical Phased Arrays	96
4.2.1	Far-Field Distribution	97
4.2.2	Experimental Results	98
4.2.3	Effect of Residual Phase Noise on Fringe Visibility	100
5	The Optoelectronic Swept-Frequency Laser	106
5.1	Introduction	106
5.2	System Description	107
5.2.1	Small-Signal Analysis	110
5.2.2	Predistortion of the SCL Bias Current	112
5.3	Experimental Demonstration	114
5.3.1	Linear Frequency Sweep	114
5.3.1.1	Distributed Feedback SCL	114
5.3.1.2	Vertical Cavity Surface-Emitting Laser	116
5.3.2	Arbitrary Frequency Sweeps	118
5.4	Range Resolution of the Optoelectronic SFL	119
5.5	Label-Free Biomolecular Sensing Using an Optoelectronic SFL	122
6	Extending the Bandwidth of SFLs	129
6.1	Chirp Multiplication by Four-Wave Mixing	129
6.1.1	Theory	130
6.1.1.1	Bandwidth-Doubling by FWM	130
6.1.1.2	Bandwidth Limitations due to Dispersion	134
6.1.1.3	Quasi-Phase-Matching Using Alternating Dispersions	136
6.1.2	Experiment	140

6.1.2.1	Chirp Bandwidth-Doubling	140
6.1.2.2	Dispersion Compensation	142
6.1.3	Bandwidth Extension	147
6.2	Multiple Source FMCW Reflectometry	151
6.2.1	MS-FMCW Analysis	151
6.2.2	Stitching	155
6.2.3	Experimental Results	159
6.2.4	Summary	161
7	Conclusion	163
7.1	Summary of the Thesis	163
7.2	Outlook	165
A	Residual Phase Error in an OPLL with Nonuniform FM Response	168
B	Four-Wave Mixing in a Multisegment Nonlinear Waveguide	173
	Bibliography	177

List of Figures

1.1	Schematic diagram of a generic phase-locked loop.	2
1.2	A frequency-modulated continuous wave (FMCW) experiment.	4
2.1	A heterodyne semiconductor laser optical phase-locked loop.	9
2.2	(a) Schematic diagram of an OPLL. (b) Linearized small-signal model for phase noise propagation in the OPLL.	10
2.3	Simplified schematic diagram of an OPLL.	16
2.4	Bode plots for (a) a Type I OPLL and (b) a Type I OPLL with a propagation delay of 10 ns. The phase-crossover frequency is indicated by the marker in (b).	18
2.5	Type I, second-order OPLL using an active filter.	20
2.6	Variation of the minimum variance of the phase error as a function of the normalized gain for a Type I OPLL in the presence of propagation delay.	22
2.7	Variation of (a) the π -crossover frequency \bar{f}_π and (b) the maximum stable loop gain $\bar{K}_{L,max}$ as a function of the position of the loop zero $\bar{\tau}_0$, for a Type II OPLL in the presence of a delay τ_L	24
2.8	Variation of the minimum variance of the phase error as a function of the parameter $\bar{\tau}_0$, for a Type II OPLL with delay τ_L	25
2.9	Experimentally measured FM response of a commercial DFB laser with a theoretical fit using a low-pass filter model.	26
2.10	Bode plots for (a) a Type I OPLL including the SCL FM response, and (b) the same response with an additional lead filter.	30

2.11	Practical OPLL configuration, including a lead filter to increase the phase-crossover frequency and a low frequency active lag filter (implemented by the parallel arm) to increase the hold-in range.	31
2.12	Phase-locking results using various commercially available SCLs.	34
2.13	Cartoon representation of the phase response of a single-section SCL showing the regimes of operation of a conventional OPLL and a sideband-locked OPLL.	36
2.14	Schematic diagram of a heterodyne sideband-locked OPLL.	37
2.15	Measured FM response of the DFB SCL used in the sideband locking experiment.	39
2.16	Beat spectrum between the locked sideband of the slave SCL and the master laser.	40
2.17	Lineshape measurements of the master laser, free-running and phase-locked optical sideband of the slave SCL, using a delayed self-heterodyne interferometer with a frequency shift of 290 MHz.	41
2.18	(a) Schematic diagram of the double-loop configuration. (b) Linearized small-signal model for phase propagation.	43
2.19	(a) Schematic diagram of the composite heterodyne OPLL. (b) Linearized small-signal model for phase propagation.	46
2.20	Experimentally measured frequency modulation of a single-section distributed feedback semiconductor laser and theoretical fit using equation (2.40).	48
2.21	Calculated two-sided spectral densities of the residual phase error in the loop, according to equations (2.18), (2.56) and (2.60). The variance of the phase error is the area under the curves.	50
2.22	Measured spectrum of the beat signal between the optical output and the master laser for an SCL in (a) a heterodyne OPLL, and (b) a double-loop feedback system shown in figure 2.18.	52

2.23	Measured spectrum of the beat signal between the optical output and the master laser for an SCL in (a) a heterodyne OPLL, and (b) a composite PLL shown in figure 2.19.	53
3.1	Individual SCLs all lock to a common narrow-linewidth master laser, thus forming a coherent array. An offset RF signal is used in each loop for additional control of the optical phase.	56
3.2	Measured linewidths of the master fiber laser, and the free-running and phase-locked slave SCL.	58
3.3	Measured frequency noise spectra of the master fiber laser, and the free-running and phase-locked slave DFB semiconductor laser. The green curve is the theoretical calculation of the frequency noise spectrum of the phase-locked slave laser using equation (3.1) and the measured loop parameters.	59
3.4	Delayed self-heterodyne interferometer experiment	60
3.5	Model of the power spectral density of the frequency noise of the master laser and the free-running and locked slave laser. The OPLL is assumed to be “ideal” with a loop bandwidth f_L	62
3.6	Variation of the accumulated phase error variance $\sigma_{\Delta\phi}^2(T_d)$ vs. interferometer delay time T_d for various values of the loop bandwidth f_L	65
3.7	Spectral density of the optical field for different values of the loop bandwidth f_L , calculated using equation (3.15).	67
3.8	Spectral density of the detected photocurrent in a delayed self heterodyne experiment using the free-running slave laser, the phase-locked slave laser, and the master laser, for different values of the interferometer delay T_d	71
3.9	Spectrum of the beat signal between the phase-locked slave SCL and the master laser.	75

3.10	Measured Allan variance of the beat signal between the slave and master lasers for the locked and unlocked cases. The variance of the RF offset signal is also shown.	76
3.11	Measured Allan variance of the beat signal between the phase-locked slave laser and the master laser, and the theoretical calculation based on equation (3.38).	78
3.12	Residual phase error calculated from the measured Allan variance using equation (3.41).	80
4.1	Coherent power-combining scheme using heterodyne SCL-OPLLs. Individual SCLs all lock to a common master laser, thus forming a coherent array. The outputs of the individual lasers are coherently combined to obtain a high power single-mode optical beam.	83
4.2	(a) Coherent combination schematic. (b) Experimentally measured combined power using two high power MOPAs as slave lasers phase-locked to a common master laser.	85
4.3	(a) Schematic of the coherent combination experiment with additional electronic phase control. (b) Experimentally measured combined power using External Cavity SCLs at 1064 nm, without and with the VCO loop connected.	87
4.4	Steady-state model for the loop OPLL 2 shown in figure 4.3(a).	89
4.5	Small-signal phase model for the power-combining scheme with the additional VCO loop.	92
4.6	Binary tree configuration for the power combination of a number of SCLs locked to a common master laser in the filled-aperture configuration.	94
4.7	A one-dimensional array of coherent optical emitters.	97
4.8	Experimental setup for the demonstration of beam-steering using OPLLs.	99

4.9	Measured far-field intensities on the infrared camera for $d_s = 0.25$ mm, when (a) one of the OPLLs is unlocked and (b), (c) both OPLLs are locked. The RF phase is varied between (b) and (c), demonstrating electronic steering of the optical beam.	100
4.10	Horizontal far-field intensity distributions demonstrating beam-steering of half a fringe by an RF phase shift of π radians, for emitter spacings of (a) $d_s = 0.25$ mm and (b) $d_s = 0.5$ mm. The incoherently added intensity distribution is also shown in (a).	101
4.11	Comparison of the experimental far-field intensity distribution with the theoretical calculation.	102
4.12	Separation between fringes as a function of the inverse beam separation d_s^{-1} , compared to theory.	102
5.1	Optoelectronic feedback loop for the generation of accurate broadband linear chirps. The optical portion of the loop is shown in blue.	108
5.2	Small-signal phase propagation in the optoelectronic SFL feedback loop.	111
5.3	Measured spectrograms of the output of the loop photodetector, for the (a) free-running and (b) predistorted cases. The predistortion significantly reduces the SCL nonlinearity. The delay of the MZI is $\tau = 28.6$ ns.	113
5.4	Measured spectrogram of the output of the loop photodetector when the loop is in lock, showing a perfectly linear optical chirp with slope 100 GHz/ms. (b) Fourier transform of the photodetector output measured over a 1 ms duration.	115
5.5	Measured optical spectrum of the locked swept-frequency SCL. RBW = 10 GHz.	116
5.6	Experimental demonstration of generation of a perfectly linear chirp of 500 GHz / 0.1 ms using a VCSEL. (a), (b), and (c) Spectrograms of the optical chirp slope for a ramp input, after iterative predistortion and the phase-locked SFL respectively. (d) Measured optical spectrum.	117

5.7	Measured spectrograms of the output of the loop photodetector, illustrating arbitrary sweeps of the SCL frequency. (a) The reference signal is swept linearly with time. (b) The reference signal is swept exponentially with time. The laser sweep rate varies between 50 and 150 GHz/ms.	119
5.8	Schematic diagram of an FMCW ranging experiment with a linearly chirped optical source.	120
5.9	Range resolution measurements using the optoelectronic swept-frequency VCSEL.	121
5.10	High- Q mode of a silica microtoroid in air, measured using an optoelectronic SFL at 1539 nm.	124
5.11	Whispering gallery mode resonances of a microtoroid in water, measured using optoelectronic SFLs at (a) 1539 nm and (b) 1310 nm.	125
5.12	Specific sensing of 8-isoprostane using a microtoroid resonator and an optoelectronic SFL at 1310 nm.	127
6.1	(a) Schematic diagram of the four-wave mixing (FWM) experiment for chirp bandwidth-doubling. (b) Spectral components of the input and FWM-generated fields. The chirp-doubled component is optically filtered to obtain the output waveform.	131
6.2	Output power as a function of the input frequency difference, for different values of fiber length and input power ($P_{ch} = P_R = P$). The dispersion, loss and nonlinear coefficient of the fiber are described in the text.	135
6.3	(a) Multisegment waveguide for quasi-phase-matching. The evolutions of the output field $A_{out}(z)$ along the waveguide for one and two segments are shown in (b) and (c) respectively.	137
6.4	Comparison of the generated FWM field in a structure with 3 segments of lengths L each and alternating dispersions of $\pm D_c$, with a single segment of length $3L$ and dispersion $+D_c$	139

6.5	Schematic diagram of the experimental setup for the demonstration of chirp bandwidth-doubling by four-wave mixing.	141
6.6	Experimental demonstration of bandwidth-doubling by FWM.	141
6.7	Measured slopes of the (a) input and (b) output optical chirps demonstrating the doubling of the optical chirp slope by FWM.	143
6.8	Improvement in the FWM power using a two-segment HNLF.	144
6.9	Theoretically calculated output power as a function of the input frequency difference for the two-segment dispersion compensated HNLF, compared to the same lengths ($L_{tot} = 200$ m) of individual fibers.	145
6.10	Experimental demonstration of improved bandwidth using a quasi-phase-matched nonlinear fiber.	145
6.11	Comparison of the normalized experimentally measured FWM power in two individual segments of 100 m each with opposite signs of the dispersion parameter, and the dispersion-compensated two-segment fiber.	147
6.12	Cascaded FWM stages for geometric scaling of the chirp bandwidth. Each stage consists of a coupler, amplifier, HNLF and filter as shown in figure 6.1(a).	148
6.13	Spectral components in a bandwidth tripling FWM experiment using two chirped optical inputs.	149
6.14	(a) FWM “engine” for geometric scaling of the chirp bandwidth. The filter is switched every T seconds so that it passes only the FWM component generated. (b) Output frequency vs. time.	150
6.15	(a) Schematic diagram of an FMCW ranging experiment with a linearly chirped optical source. (b) Variation of the optical frequency with time.	152
6.16	Illustration of the MS-FMCW concept.	156
6.17	Schematic of a multiple source FMCW ranging experiment. A reference target is imaged along with the target of interest, so that the intersweep gaps may be recovered.	157
6.18	Architecture of a potential MS-FMCW imaging system.	159
6.19	Experimental MS-FMCW results using a DFB SCL.	160

6.20	Experimental MS-FMCW results using a VCSEL.	162
7.1	Schematic diagram of a potential compact integrated label-free biomolecular sensor.	166
A.1	Variation of (a) the normalized π -crossover frequency and (b) the normalized maximum gain as a function of the parameter b in equation (A.1).	169
A.2	Variation of the integral $\mathcal{I}(b, \bar{K}_F)$ in equation (A.6) as a function of \bar{K}_F , for $b = 1.64$	170
A.3	Variation of the (a) normalized optimum gain $\bar{K}_{F,opt} = K_{F,opt}/f_c$ and (b) the normalized minimum residual phase error $\sigma_{min}^2 f_c / (\Delta\nu_m + \Delta\nu_s)$ as a function of the parameter b , for a first-order OPLL with a SCL with nonuniform FM response.	171
B.1	A multisegment nonlinear waveguide for four-wave mixing.	174

List of Tables

1.1	Comparison between electronic PLLs and OPLLs	3
2.1	Parameters of OPLLs demonstrated using commercially available SCLs	32
2.2	Parameters and results of the numerical calculations of the performance of composite OPLLs	50
6.1	Length of HNFLF and input power requirements for different output bandwidths and power levels	136

Glossary of Acronyms

CBC Coherent beam-combining

CCO Current-controlled oscillator

DFB Distributed feedback

EDFA Erbium-doped fiber amplifier

FM Frequency modulation

FMCW Frequency modulated continuous wave

FWHM Full width at half maximum

FWM Four-wave mixing

GVD Group velocity dispersion

HNLF Highly nonlinear fiber

LIDAR Light detection and ranging

MOPA Master oscillator power amplifier

MS-FMCW Multiple source-frequency modulated continuous wave

MZI Mach-Zehnder interferometer

OCT Optical coherence tomography

OPLL Optical phase-locked loop

PD Photodetector

PLL Phase-locked loop

RIN Relative intensity noise

RF Radio frequency

SCL Semiconductor laser

SFL Swept-frequency laser

SS-OCT Swept source-optical coherence tomography

VCO Voltage-controlled oscillator

VCSEL Vertical cavity surface-emitting laser

VECSEL Vertical external cavity surface-emitting laser